Editors' Suggestion

Multivalley Electron Conduction at the Indirect-Direct Crossover Point in Highly Tensile-Strained Germanium

M.B. Clavel,[1] F. Murphy-Armando,[2,*] Y. Xie,[3] K.T. Henry,[4] M. Kuhn,[4] R.J. Bodnar,[5] G.A. Khodaparast,[3] D. Smirnov,[6] J.J. Heremans,[3] and M.K. Hudait[1,†]

[1] *Advanced Devices & Sustainable Energy Laboratory (ADSEL), Bradley Department of Electrical and Computer Engineering, Virginia Tech, Blacksburg, Virginia 24061, USA*
[2] *Tyndall National Institute, University College Cork, Lee Maltings, Dyke Parade, Cork, Ireland*
[3] *Department of Physics, Virginia Tech, Blacksburg, Virginia 24061, USA*
[4] *Intel Corporation, Hillsboro, Oregon, USA*
[5] *Fluids Research Laboratory, Department of Geosciences, Virginia Tech, Blacksburg, Virginia 24061, USA*
[6] *National High Magnetic Field Laboratory, Tallahassee, Florida 32310, USA*

(Received 24 September 2020; revised 2 September 2022; accepted 17 November 2022; published 27 December 2022)

As forward-looking electron devices increasingly adopt high-mobility low-band-gap materials, such as germanium (Ge), questions remain regarding the feasibility of strain engineering in low-band-gap systems. Particularly, the Ge L-Γ valley separation ($\sim$150 meV) can be overcome by introducing a high degree of tensile strain ($\varepsilon \geq 1.5\%$). It is therefore essential to understand the nature of highly strained Ge transport, wherein multivalley electron conduction becomes a possibility. Here, we report on the competitiveness between L- and Γ-valley transport in highly tensile-strained ($\varepsilon \sim 1.6\%$) Ge/$In_{0.24}Ga_{0.76}As$ heterostructures. Temperature-dependent magnetotransport analysis reveals two contributing carrier populations, identified as lower- and higher-mobility L- and Γ-valley electrons (in Ge), using temperature-dependent Boltzmann transport modeling. Coupling this interpretation with electron-cyclotron-resonance studies, the effective mass (m^*) of the higher-mobility Γ-valley electrons is probed, revealing $m^* = (0.049 \pm 0.007)m_e$. Moreover, a comparison of empirical and theoretical m^* indicates that these electrons reside primarily in the first-two quantum sublevels of the Ge Γ valley. Consequently, our results provide an insight into the strain-dependent carrier dynamics of Ge, offering alternative pathways toward efficacious strain engineering.

DOI: 10.1103/PhysRevApplied.18.064083

I. INTRODUCTION

Epitaxial and process-induced strain have been used to enhance the electronic transport properties of silicon (Si) metal-oxide-semiconductor field-effect transistors (MOSFETs) for over a decade [1,2]. In particular, silicon-germanium ($Si_{1-x}Ge_x$) alloy source-drain stressors [3,4] and virtual substrates [5] have been utilized to apply compressive strain to the Si channel in p-MOSFETs, enhancing hole mobility in proportion to the Si/$Si_{1-x}Ge_x$ lattice mismatch (i.e., strain, ε). More recently, narrow-band-gap semiconductors, such as germanium (Ge) and III-V ternary alloys (e.g., $In_xGa_{1-x}As$), have attracted significant attention due to their enhanced electron and hole mobilities, as compared to Si [6–10]. Similar to Si-based FET architectures, epitaxial and process-induced strain have also been proposed as methods for enhancing the electronic transport properties of high-mobility semiconductors [11, 12]. Whereas current research predominately focuses on the demonstration of strained Ge (or $In_xGa_{1-x}As$) FETs [13–15], comparatively little effort [16] is dedicated to elucidating the effects of high-strain states on the electronic transport properties of strained Ge (ε-Ge) materials. Moreover, the difficulty of such an investigation is compounded by Ge's pseudodirect-band-gap nature, wherein a difference of only about 150 meV separates the L- and Γ-valley conduction-band minima [11,17–19]. Thus, at high-strain states ($\varepsilon \geq 1.5\%$) [18,19], strain-induced modification of the Ge band structure is expected to lower the Γ-valley conduction-band minimum below that of the L valley, thereby transitioning Ge into a direct-band-gap material with the potential for competitive behavior between the two conduction-band minima to arise [20,21]. However, the density of states (DOS) mass in the L and Γ valley without strain are $m_L^{\mathrm{DOS}} = 0.22\ m_e$ and $m_\Gamma^{\mathrm{DOS}} = 0.05\ m_e$ at room temperature, respectively (m_e denotes the

*philip.murphy@tyndall.ie
†mantu.hudait@vt.edu

 © 2022 American Physical Society

free-electron mass). The DOS mass in the L valley does not change appreciably, and the Γ-valley DOS mass is reduced from 0.05 m_e at 0% strain to 0.04 m_e at 1.6% biaxial tensile strain. Therefore, the carriers can presumably stay within the L valley, and by increasing doping along with tensile strain, one can transfer the carriers from the L valley to the Γ valley. To achieve carrier transport through the Γ valley, it needs to be separated in energy from the L valley by several tens of meV. Decoupling of the carrier density and mobility from these two valleys as a function of biaxial tensile strain is still elusive, to date, especially enhancement of the mobility for L electrons. By applying a biaxial tensile strain of about 1.6%, indirect-band-gap Ge is converted into a direct band gap, as demonstrated theoretically using $\mathbf{k}\cdot\mathbf{p}$ and experimentally [21–23] by low-temperature photoluminescence and photoreflectance measurements. At this strain level, electrons with high mobility can begin to populate the Γ valley, and thus, decoupling of carriers and their mobility is a significant challenge. Thus, the strain-enhanced mobility in ε-Ge and relative proportion of carriers in each valley as a function of strain and temperature are of importance. This transport study can find several applications, where carrier density, band offset for carrier confinement, and strain level, which enhance mobility, are all needed for low-power tunnel transistor [24,25], tunnel FET-based memory and logic device [26,27], laser [21,28–30], spintronic [31,32], and qubit [33] applications. In addition, there could be an application in single-electron and quantum devices as well as in cryoelectronics, in which the Γ-electron participation studied here is relevant.

To shed light on these issues, this work exploits the ability of group IV and III-V heterostructures to induce modular tunable epitaxial stress in Ge thin films provided by an underlying III-V strain stressor [25,34,35], thereby enhancing the electronic transport properties of the strained epitaxial Ge layers in a controlled fashion. Utilizing a dual-chamber vacuum-interconnected molecular-beam-epitaxy (MBE) system, we demonstrate the feasibility of integrating low-defect atomically abrupt tensile-strained ε-Ge/In$_x$Ga$_{1-x}$As heterostructures on lattice-mismatched (001)GaAs substrates. Further characterization of the thin-film ε-Ge electronic transport properties and an independent, combined first-principles, and Boltzmann transport calculation framework reveal directly multivalley (i.e., L and Γ valleys) conduction in the ε-Ge material system. The temperature dependence of the calculated mobility and carrier contributions in the L and Γ valleys of ε-Ge are compared with the experimentally measured results. We also present the direct probing of carrier effective mass in ε-Ge under biaxial tensile stress, and from these results, provide evidence for the transition from an indirect to a direct band gap in tensile-strained Ge thin films.

TABLE I. Information on unstrained Ge/AlAs and tensile-strained Ge/In$_{0.16}$Ga$_{0.84}$As and Ge/In$_{0.24}$Ga$_{0.76}$As heterostructures.

Heterostructure	Strain (%)	Ge thickness (nm)
Ge/AlAs/(100)2° GaAs	0	270
Ge/In$_{0.16}$Ga$_{0.84}$As/In$_x$Ga$_{1-x}$As/(100)2° GaAs	0.75	15
Ge/In$_{0.24}$Ga$_{0.76}$As//In$_x$Ga$_{1-x}$As/(100)2° GaAs	1.6	30

II. METHODS

A. Synthesis and characterization of materials

The unintentionally doped epitaxially unstrained Ge/AlAs and tensile-strained Ge/In$_x$Ga$_{1-x}$As (0.75% and 1.6%) heterostructures are grown using an *in situ* dual-chamber MBE growth process. Separate III-V and IV reactors connected *via* an ultrahigh-vacuum transfer chamber allow for isolated growth phases for the In$_{0.24}$Ga$_{0.76}$As (AlAs, In$_{0.16}$Ga$_{0.84}$As) and unstrained Ge or ε-Ge layers, thereby minimizing the likelihood of atomic interdiffusion at the ε-Ge/In$_{0.24}$Ga$_{0.76}$As heterointerface (or ε-Ge/In$_{0.16}$Ga$_{0.84}$As) as well as during ε-Ge growth. The initial (001) GaAs substrate is offcut 2° towards the ⟨110⟩ direction and desorbed of native oxide at 750 °C under an arsenic (As) overpressure of about 10^{-5} Torr. Here, the (100)/2° GaAs substrate is used for efficient strain relaxation of the graded In$_x$Ga$_{1-x}$As buffer layer, which is important for subsequent ε-Ge layer growth. The substrate offcut along with growth parameters (growth temperature, growth rate, grading rate, substrate conductivity, etc.) are used to relax the strain energy from the In$_x$Ga$_{1-x}$As graded buffer to create a virtual substrate (or template) for subsequent layer growth. Reflection high-energy electron diffraction is used to analyze the surface before, during, and after growth. In the case of the 1.6% ε-Ge sample, 0.25 μm of GaAs is grown at 650 °C, followed by a 1-μm linearly graded In$_x$Ga$_{1-x}$As buffer and 500-nm In$_{0.24}$Ga$_{0.76}$As stressor grown at 550 °C. The ultrathin 30-nm ε-Ge layer is grown at 400 °C using a 0.025 μm/h growth rate to maintain heterointerface abruptness. The growth temperature and growth rate for all other Ge samples are kept constant. Complete details of the growth procedure can be found elsewhere [25]. Table I shows each Ge/III-V heterostructure studied in this work.

Subsequent characterization of the heterostructure's crystal quality, empirical In$_x$Ga$_{1-x}$As stressor composition, and epilayer relaxation and strain states is accomplished using high-resolution x-ray diffraction (HRXRD).

The x-ray rocking curves and reciprocal space maps are recorded using a PANalytical X-pert Pro system equipped with PIXcel and proportional detectors and a monochromatic Cu $K\alpha$ ($\lambda = 1.540\,597$ Å) x-ray source. A JY Horiba LabRam HR800 system equipped with a 514.32-nm Ar laser source is used for the collection of Raman spectra and independent corroboration of the ε-Ge epitaxial strain. Atomic force microscopy (AFM) micrographs collected with a Bruker Dimension Icon AFM instrument in tapping mode are utilized to analyze the surface morphology of the ε-Ge/$In_{0.24}Ga_{0.76}As$ heterostructure. Further structural characterization by way of high-resolution cross-section transmission electron microscopy (HRTEM) is performed on a JEOL 2100 TEM instrument and reveals the structural quality, ε-Ge/$In_{0.24}Ga_{0.76}As$ heterointerface uniformity, and lattice coherence at the strained layer-stressor heterointerface. Additional atomic scale characterization of the ε-Ge/$In_{0.24}Ga_{0.76}As$ interface is performed *via* atomic probe tomography (APT), a combination of time-of-flight spectroscopy and atomic projection imaging that allows for the reconstruction of atomically accurate three-dimensional (3D) ion maps of selected regions of material. Optimization of the measurement conditions utilized herein begins by cooling of the sample to 50 K, followed by a reduction of the laser pulse energy to 3 pJ at a pulse frequency of 250 kHz. The resultant detection rate, approximately 0.01 ions/pulse, is maintained throughout the analysis. We note that the analysis is performed parallel to the ⟨001⟩ growth direction. The commercially available IVAS™ software is used in the reconstruction of the 3D ion maps.

B. Electronic and magnetotransport analysis

The unstrained and highly tensile-strained Ge magnetotransport properties, including carrier density and mobility, are measured using Hall measurements under the van der Pauw geometry. In-Sn Ohmic contacts are alloyed on the Ge surface to ensure low-resistance stable electrical contacts at cryogenic temperatures. Temperature-dependent magnetotransport measurements are performed from 0.36 to 5.63 K in magnetic fields up to ±9 T using a ^{3}He cryostat and liquid ^{3}He submersion and sample-in-vapor cooling. Carrier effective masses for the ε-Ge/$In_{0.24}Ga_{0.76}As$ heterostructure are extracted from the temperature dependence of Shubnikov-de Haas oscillations in magnetotransport data and independently confirmed *via* electron-cyclotron-resonance analysis. The magnetotransmission measurements necessary for probing the cyclotron-resonance response of the ε-Ge/$In_{0.24}Ga_{0.76}As$ heterostructure are carried out at the National High Magnetic Field Laboratory using a Fourier-transform infrared spectrometer, superconducting magnet, Globar emission source, and Si bolometer detector.

C. Calculation of the Ge electronic transport properties under tensile stress

The electronic and band-structure properties of the ε-Ge/$In_xGa_{1-x}As$ heterostructures are theoretically investigated using first-principles calculations that include the effect of strain on Ge material properties. The calculations follow the approach taken by one of the authors for the calculation of transport in $Si_{1-x}Ge_x$ alloys and strained Ge nanostructures, with the addition of changes to the proportion of transport in each valley due to the presence of the ($In_xGa_{1-x}As$ layer, as explained below. The resulting material parameters are used with the Boltzmann transport equation to determine the *n*-type carrier mobility in the ε-Ge layers and examine the population distribution of carriers between the L and Γ valleys of Ge. The electron–phonon-scattering matrix elements in ε-Ge are calculated using first-principles density-functional perturbation theory for intervalley scattering and the frozen-phonon approach for intravalley scattering by acoustic phonons, as in Refs. [20,36] for strained Ge and $Si_{1-x}Ge_x$. The effects of ionized-impurity scattering are included using the Brooks-Herring approach [37–40]. To ease integration of the transport properties across the Brillouin zone under different strain conditions, we use the first-principles-based **k·p** analytical form of the electronic band structure of ε-Ge after Rideau *et al*. [17]. This **k·p** approach, unlike the local density approximation in density-functional theory, gives the correct electronic energy gap and dispersion. We correct the temperature dependence of the energy gap and dispersion following the approach of Ref. [37] for strained $Si_{1-x}Ge_x$ (including Ge). The temperature- and alloy-content-dependent mobility of $In_xGa_{1-x}As$ is obtained from reported experimental values [41].

The effects of quantum confinement follow an envelope-function approach [42], with the boundary conditions given by the empirical ε-Ge/$In_xGa_{1-x}As$ band offsets reported in Ref. [25]. To simplify the calculation, we approximate the heterostructure by a mirror-symmetric $In_xGa_{1-x}As$/Ge/$In_xGa_{1-x}As$ structure, rather than the uncapped case of the experiment. Due to the large band offsets, this approximation allows for much faster computation with little sacrifice to accuracy. The presence of air rather than $In_xGa_{1-x}As$ at one end would shift the wave function slightly towards $In_xGa_{1-x}As$, due to the larger Ge-air band offset. Because the wave function in the $In_xGa_{1-x}As$ region is so small, we expect the effect on mobility to be very small.

The contribution to the mobility from the Ge L and Γ valleys and the $In_xGa_{1-x}As$ Γ valley is given by

$$\mu_{\text{Ge/In}_{0.24}\text{Ga}_{0.76}\text{As}} = r_{\text{In}_x\text{Ga}_{1-x}\text{As}}\mu_{\text{In}_x\text{Ga}_{1-x}\text{As}} + r_{\text{Ge}^\Gamma}\mu^{\Gamma}_{\text{Ge}} + r^{L}_{\text{Ge}}\mu^{L}_{\text{Ge}}, \quad (1)$$

where μ_i^j is the calculated contribution to the mobility from material i and valley j, and r_i^j is the proportion of carriers in valley j of material i, as given by

$$r_i^j = n^j / n_T \sum_b \int_i dz |\psi_b^j(z)|^2, \quad (2)$$

where $\psi_b^j(z)$ is the z-direction part of the separable envelope wave function of subband b of valley j, and the integral runs only in coordinate z inside material i. Coordinate z denotes the growth and confinement direction. The number of carriers in valley j is n^j, out of a total of $n_T = n^{\mathrm{Ge}} + n^{\mathrm{In}_x\mathrm{Ga}_{1-x}\mathrm{As}}$ carriers.

III. RESULTS

A. Structural properties and relaxation dynamics of the ε-Ge/$In_{0.24}Ga_{0.76}As$ system

A cross-section schematic diagram of the ε-Ge/$In_{0.24}Ga_{0.76}As$ heterostructure investigated herein is presented in the left inset of Fig. 1(a). Similarly, the right inset of Fig. 1(a) illustrates the impact of epitaxially induced tensile strain on the (expanded) in-plane and (compressed) out-of-plane lattice constants, a and c, respectively, of a coherently strained epilayer (i.e., $a_{\mathrm{epi}}=a_{\mathrm{stressor}}$). When utilizing $In_xGa_{1-x}As$ as a stressor, tailoring of the InAs mole fraction, and therefore, $a_{\mathrm{In}_x\mathrm{Ga}_{1-x}\mathrm{As}}$, enables modulation of the lattice strain imparted to an overlying lattice-mismatched film, e.g., Ge. In turn, the electronic and optical properties of the overlying strained epilayer can be tuned within a wide range by varying the amount of strain. As such, a target InAs mole fraction of 0.24 is selected for this work, corresponding to a nominal tensile strain of about 1.63% with respect to relaxed Ge. Such a high-Ge-strain state is predicted to lower the Ge Γ-valley conduction-band minimum below that of the L valley, resulting in a direct-band-gap Ge material [11,12,18,19].

HRXRD data (Fig. 1) of the as-grown heterostructure reveal that the Ge epilayer is indeed pseudomorphic with respect to the $In_xGa_{1-x}As$ virtual substrate (VS). As shown by the symmetric (004) rocking curve (RC) in Fig. 1(a), the strain-induced compression of c_{Ge} is observed directly as an increase in the (004) Bragg angle of the ε-Ge film (red). For comparison, the (004) RC from a quasi-lattice-matched Ge/GaAs heterostructure is also shown (blue), emphasizing the resultant angular separation between the ε-Ge and relaxed Ge diffraction peaks due to strain incorporation. We note that the Pendellösung oscillations observed in the Ge/GaAs RC are not observed on the ε-Ge/$In_xGa_{1-x}As$ heterostructure, likely owing to disorder-induced x-ray scattering within the dislocation filtering $In_xGa_{1-x}As$ linearly graded buffer (LGB) and a thicker excitation volume in the relaxed Ge material rather than a nonabrupt ε-Ge/$In_xGa_{1-x}As$ heterointerface.

In addition, symmetric (004) and asymmetric (115) reciprocal-space-map (RSM) analysis permits further characterization of the Ge-epilayer-strain state, InAs mole fraction of the $In_xGa_{1-x}As$ VS, and relaxation state of the metamorphic buffer. Figures 1(b) and 1(c) show the recorded (004) and (115) RSMs, respectively, highlighting the reciprocal-lattice-point (RLP) centroid for each layer. The Qx-Q_z symmetry of the ε-Ge RLP suggests uniform crystallinity absent of mosaicity- or defect-related scattering, thereby implying a lack of observable relaxation with the ε-Ge epilayer. Likewise, the narrow symmetric nature of the $In_xGa_{1-x}As$ VS RLP indicates dislocation-minimal constant-composition epitaxy, signifying a strong confinement of lattice-mismatch-induced defects in the metamorphic LGB and a high amount of buffer relaxation. These observations are quantified following the procedures outlined in Refs. [43,44], as summarily reported in Ref. [25], yielding an $In_xGa_{1-x}As$ stressor InAs mole fraction, $x_{\mathrm{expt.}}$, of 0.237. From the about 540 arcsec tilt determined *via* the (004) reflection, it can be posited that buffer relaxation

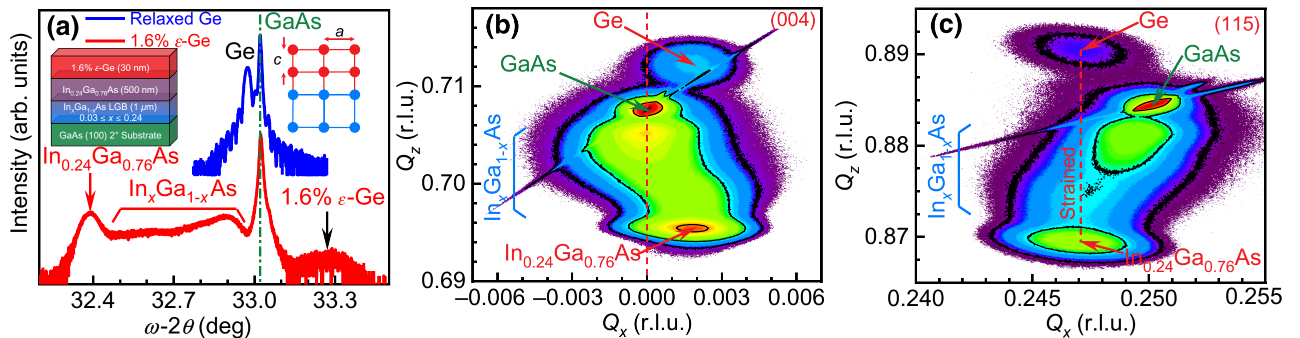

FIG. 1. (a) Symmetric (004) ω-2θ HRXRD spectra of as-grown ε-Ge/$In_{0.24}Ga_{0.76}As$ heterostructure (red), as compared to a quasi-lattice-matted Ge/GaAs (001) heterostructure (blue). Right inset demonstrates out-of-plane lattice contraction due to corresponding in-plane lattice expansion, whereas left inset provides a cross-section schematic of the ε-Ge/$In_{0.24}Ga_{0.76}As$ heterostructure. High-resolution reciprocal space maps taken along (b) symmetric (004) and (c) asymmetric (115) crystallographic orientations, where (r.l.u) is reciprocal lattice unit.

occurs in a partially asymmetric nature [45], which is further confirmed *via* the presence of minute, but quantifiable, asymmetries in the $[1\bar{1}0]$- and [110]-oriented surface morphology of the ε-Ge/$In_{0.24}Ga_{0.76}As$ heterostructure (see Sec. I and Fig. S1 within the Supplemental Material [46–49]). Moreover, the Ge film is found to be 1.6% tensile strained with respect to relaxed (bulk) Ge, indicating near-ideal stress transfer to the Ge lattice and reinforcing the nature of the ε-Ge RLP previously discussed.

Raman spectroscopic data (Fig. 2) further confirm the nature of the ε-Ge epilayer strain, as demonstrated by the frequency shift observed in the measured ε-Ge/$In_{0.24}Ga_{0.76}As$ Raman spectra. As can be seen in Fig. 2, the ε-Ge epilayer (red) exhibits a wave-number shift ($\Delta\omega$) of -6.53 cm^{-1} with respect to the Raman spectra taken from a (001)Ge substrate (blue), resulting in a strain value of $\varepsilon_{\parallel} = 1.57\%$ [50]. This value is found to be in good agreement with the theoretical misfit for the ε-Ge/$In_{0.24}Ga_{0.76}As$ heterostructure, $f \sim 1.63\%$. Additionally, the relationship between the measured $\Delta\omega$ and XRD-determined strain ($\varepsilon_{\parallel}^{XRD}$) is shown in the inset of Fig. 2. Also shown is the expected Raman shift as a function of strain (red) derived using the expression $\Delta\omega = -b\varepsilon_{\parallel}$ cm^{-1} (see Sec. II of the Supplemental Material [46,51–55]). Inclusion of our previously reported results for ε-Ge/$In_xGa_{1-x}As$ heterostructures grown on GaAs (circles) [50] and Si (squares) [53] substrates reveal a strong correlation between the expected $\Delta\omega$ deduced from $\varepsilon_{\parallel}^{XRD}$ and the measured Raman shift (symbols), noting that experimental variance between the measured and expected values is likely to be due to minute strain anisotropies in the ε-Ge epilayers as a consequence of the slightly asymmetric nature of the $In_xGa_{1-x}As$ VS relaxation. These results therefore highlight the applicability of Raman strain analysis to the ε-Ge system across a wide range of strain values and substrate platforms and further reinforce the strain-relaxation analysis *via* HRXRD presented earlier.

Low-magnification TEM analysis [Fig. 3(a)] provided additional insight into the relaxation dynamics of the ε-Ge/$In_{0.24}Ga_{0.76}As$ heterostructure, revealing a dense network of misfit and threading dislocations (TDs) confined within the metamorphic $In_xGa_{1-x}As$ LGB. Likewise, high-magnification TEM analysis [Fig. 3(b)] demonstrates a highly uniform interface between the ε-Ge epilayer and $In_{0.24}Ga_{0.76}As$ strain template. We note that Fig. 3(b) consists of the as-recorded micrograph superimposed with a noise-filtered image of the same, the effect of which is to enhance image contrast in the vicinity of atomic columns. Utilization of this two-step FFT noise-filtering approach [i.e., $F^{-1}(F(k))$] suggests an atomically abrupt heterointerface lacking substantial atomic interdiffusion. In the next section, we provide definitive evidence for this conclusion *via* APT. More localized FFT patterns captured from representative 14×14 nm^2 regions of the (i) ε-Ge epilayer, (ii) ε-Ge/$In_{0.24}Ga_{0.76}As$ heterointerface,

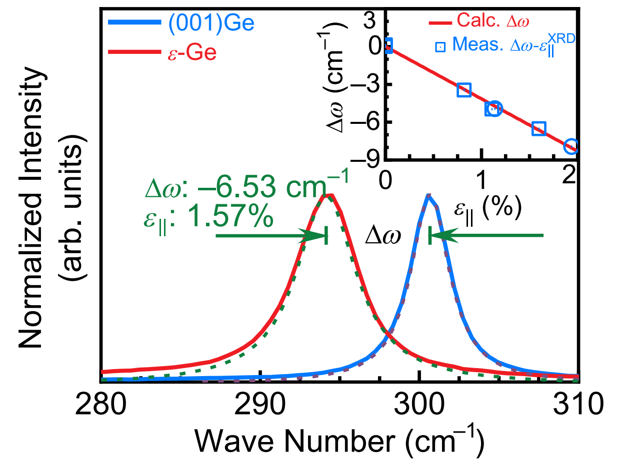

FIG. 2. Raman spectra collected for (001) Ge substrate (blue) and ε-Ge epilayer grown on $In_{0.24}Ga_{0.76}As$ (red). Inset highlights the relationship between the expected Raman wave-number shift (solid line, red) and the HRXRD-determined tensile strain (symbols, blue).

and (iii) $In_{0.24}Ga_{0.76}As$ strain template are shown in Figs. 3(c)–3(e), respectively. The indistinguishable nature of the FFT patterns across the heterointerface and the absence of satellite reflections indicate the major contribution of a single lattice parameter to the diffractogram, thereby providing ancillary support for a quasi-ideal pseudomorphic Ge epitaxy.

Figure 3(f) shows a plan-view TEM micrograph taken from a beveled sample foil (bottom-left inset) under the $g = (2\bar{2}0)$ diffraction condition. Utilizing plan-view TEM analysis permits a conservative estimation of the TD density in the $In_{0.24}Ga_{0.76}As$ stressor, $\rho_{TDD} \leq 2 \times 10^7$ cm^{-2} (see Sec. III of the Supplemental Material [46,56–59]); notably, TDs are only observed upon etching of the ε-Ge epilayer. Additionally, Fig. 3(f) reveals an abrupt termination in the $In_{0.24}Ga_{0.76}As$ misfit dislocation (MD) network, which is posited to occur at the ε-Ge/$In_{0.24}Ga_{0.76}As$ heterointerface. This is conclusively demonstrated by FFT analysis of the {111} planes in the vicinity of the interface, as shown in the insets of Fig. 3(b). MDs exhibiting the insertion of an extra half-plane of atoms (i.e., edge dislocations) are observed; notably, positive and negative edge dislocations are found in both the ε-Ge and $In_{0.24}Ga_{0.76}As$ stressor layers. Moreover, these MDs are confined to within 4 nm of the heterointerface and exhibit aperiodic MD spacing. Correlating these results with the previously discussed HRXRD analysis, the lack of quantifiable tilt in the (004) ε-Ge RLP (with respect to the $In_{0.24}Ga_{0.76}As$ stressor) suggests that these are 90° MDs. It is generally understood that, under tensile strain, it is energetically favorable for perfect 60° dislocations to disassociate into leading 90° and trailing 30° partial dislocations (see Sec. III and Fig. S2 within the Supplemental Material) [46,56]. Given the

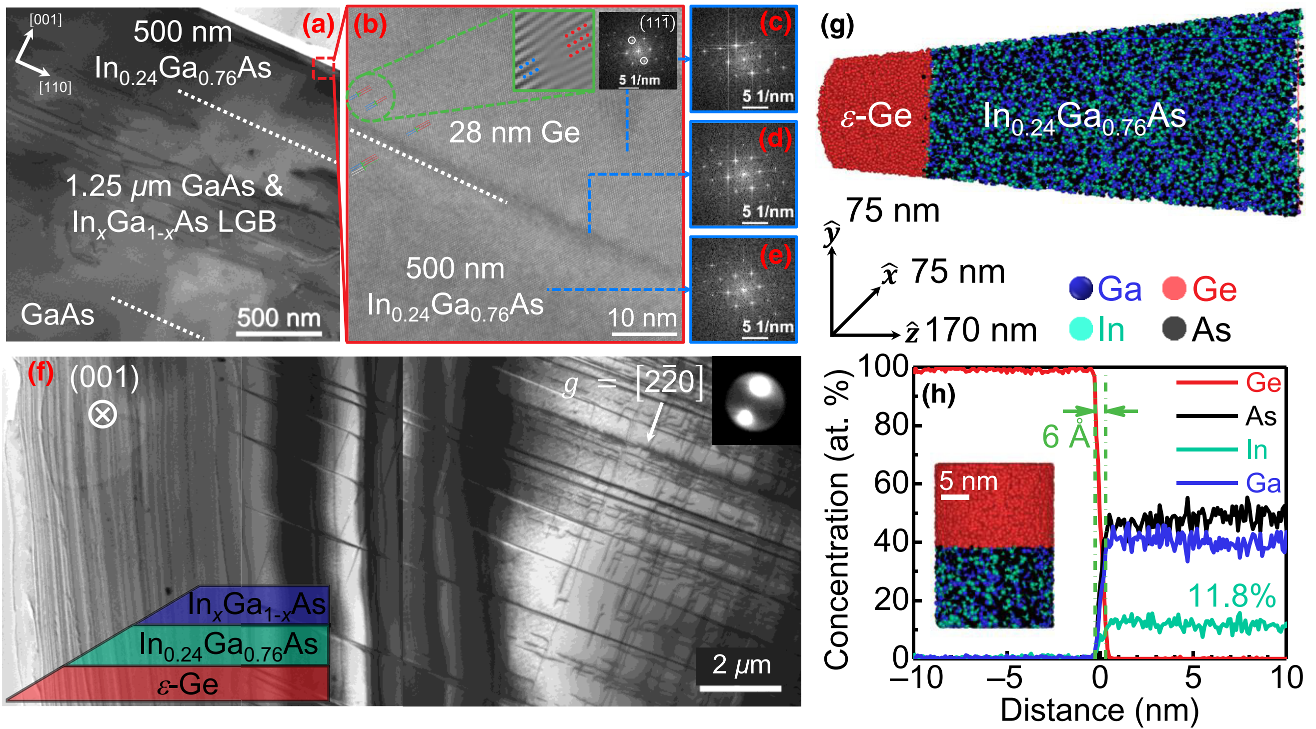

FIG. 3. (a) Low-magnification cross-section transmission electron micrograph (XTEM) of the entire ε-Ge/$In_{0.24}Ga_{0.76}As$/$In_xGa_{1-x}As$/GaAs (001) heterostructure. (b) High-magnification XTEM of the ε-Ge/$In_{0.24}Ga_{0.76}As$ heterointerface, and (c)–(e) associated fast Fourier transform (FFT) patterns. Insets display the $11\bar{1}$ crystallographic plane and corresponding reciprocal space reflections used in the misfit dislocation analysis. (f) Low-magnification plan-view TEM of a beveled ε-Ge/$In_{0.24}Ga_{0.76}As$ sample and corresponding representative cross-section schematic (bottom-left inset). (g) Reconstructed 3D atom-probe tomographic ion map of a representative $75 \times 75 \times 170$ nm^3 conical volume taken from the as-grown ε-Ge/$In_{0.24}Ga_{0.76}As$ heterostructure and (h) associated atomic concentration depth profile. Inset of (h) corresponds to the region from which the atomic concentration depth profile is generated.

irregular MD spacing observed in Fig. 3(b) and the localization of MDs in ε-Ge to corresponding dislocations in the $In_{0.24}Ga_{0.76}As$ stressor, it is therefore likely that the observed MDs are 90° partial dislocations that form during Ge epilayer growth. Indeed, a Burgers circuit traced around a representative dislocation core (see Fig. S2(d) within the Supplemental Material [46]) reveals the formation of the stacking fault associated with the nucleation of a 90° partial dislocation having a projected Burgers vector of $(a_0/6)\langle 112\rangle$. Thus, as no quantifiable ρ_{TDD} is observed in the ε-Ge epilayer, we posit that the high strain energy at the Ge surface during growth results in enhanced TD glide at the ε-Ge/$In_{0.24}Ga_{0.76}As$ heterointerface, thereby preventing vertical TD propagation and accommodating strain relaxation through the formation and disassociation of perfect 60° MDs into leading 90° partial dislocations [60].

Lastly, independent corroboration of the ε-Ge/$In_{0.24}Ga_{0.76}As$ heterointerface abruptness is provided by APT, which is used to reconstruct atomically accurate 3D ion maps of representative $75 \times 75 \times 170$ nm^3 (conical) volumes of the as-grown ε-Ge/$In_{0.24}Ga_{0.76}As$ heterostructure. Figure 3(g) shows one such reconstructed 3D ion map, wherein individual gallium (Ga), indium (In), arsenic (As), and Ge atoms are depicted in blue, green, black, and red, respectively. Likewise, a magnified region in the vicinity of the ε-Ge/$In_{0.24}Ga_{0.76}As$ heterointerface [Fig. 3(h), inset] is used to generate a representative atomic concentration depth profile [Fig. 3(h)]. Measurement of the separation between the 90% and 10% atomic thresholds for a given ion species allows for an estimation of the atomic interdiffusion at the ε-Ge/$In_{0.24}Ga_{0.76}As$ heterointerface. Explicitly, no quantifiable atomic interdiffusion occurs beyond an initial 6-Å diffuse region formed at the onset of Ge nucleation. This result can be explained by a combination of the low-temperature and low-growth-rate Ge epitaxy conditions utilized in this work. The former is expected to minimize As surface desorption from the $In_xGa_{1-x}As$ surface prior to and during Ge nucleation, whereas the latter promotes uniform Ge surface coverage during nucleation and subsequent Frank–van der Merwe-dominated epitaxy. When taken together, these two processes reduce the likelihood of As out-diffusion into the growing Ge epilayer, consequently preserving heterointerfacial uniformity and abruptness. Finally, we

note that the InAs mole fraction of the $In_xGa_{1-x}As$ virtual substrate, as determined *via* APT analysis, is 0.236 (11.8 atomic %), which is in excellent agreement with the HRXRD results outlined earlier.

B. Electronic and magnetotransport properties of highly tensile-strained Ge

Having demonstrated the successful integration of highly tensile-strained Ge on $In_xGa_{1-x}As$ strain templates, we now turn our attention to the carrier dynamics of such heterostructures. To this end, the magnetotransport properties of the ε-Ge/$In_{0.24}Ga_{0.76}As$ heterostructure are measured in a van der Pauw configuration with a magnetic field, B, applied perpendicularly to the (001) growth direction and at temperatures ranging from 0.36 to 5.63 K. Magnetotransport data consist of transverse magnetoresistance [$R_{xy}(B)$, Hall effect] and longitudinal magnetoresistance. The latter is extracted by symmetrization of data obtained for the two polarities of B, since longitudinal magnetoresistance must be symmetric with respect to applied B. Figure 4(a) presents $R_{xy}(B)$ versus B obtained at different measurement temperatures. From the slope of the linear region (over ± 2 T), an areal carrier density of $N_{S1} = 8.50 \times 10^{16}$ m^{-2} is deduced, which is substantially constant over the measured temperature range. The sign of the slope indicates that electrons are at the origin of this Hall effect. Additionally, Shubnikov-de Haas oscillations are observed at higher B, superimposed on the Hall effect, and exhibiting a pronounced dependence on temperature. The Shubnikov-de Haas oscillations are observed in this van der Pauw geometry owing to mixing of $R_{xy}(B)$ with residual longitudinal magnetoresistance. As their origin lies in longitudinal magnetoresistance, the Shubnikov-de Haas oscillations can be extracted by symmetrization in B of the data. Figure 4(b) shows the longitudinal magnetoresistance after the subtraction of a background to yield the oscillatory part (ΔR) and its subsequent normalization by the sheet resistance (R_0). The Shubnikov-de Haas oscillations exhibit a clear periodicity in inverse B, from which B^{-1} taken at the maxima versus the index of the maxima (arbitrarily starting with index 1 at $B = 0.16$ T^{-1}) is displayed in Fig. 4(c), resulting in a monotonic trend line with slope $S = (0.0853 \pm 0.001)$ T^{-1}. An areal density, N_{S2}, is deduced from S [61,62], using the relationship $N_{S2} = e/(\pi \hbar S)$, where e denotes the electron charge and $\hbar$ is Planck's constant, yielding $N_{S2} = (5.67 \pm 0.06) \times 10^{15}$ m^{-2}. Here, we assume negligible Zeeman splitting, and hence, spin degeneracy. Whether the carriers giving rise to the Shubnikov-de Haas oscillations are electrons or holes cannot be ascertained. Yet Shubnikov-de Haas oscillations require minimal broadening of Landau levels, implying that this carrier population (N_{S2}) has higher mobility than the population giving rise to the Hall effect (N_{S1}), which cannot be detected in the Shubnikov-de Haas oscillations. From the dependence on temperature of the oscillations in Fig. 4(b), an effective mass is extracted using the so-called temperature term in the description of Shubnikov-de Haas oscillations [61–63]. It is found that this effective mass is $m_2 = (0.049 \pm 0.007)m_e$, where m_e denotes the free-electron mass. From the magnetotransport measurements, it is thus concluded that two carrier populations contribute to transport: an electron population with lower mobility and higher density ($N_{S1} = 8.50 \times 10^{16}$ m^{-2}) and a population of unknown type but with higher mobility and lower density ($N_{S2} = 5.67 \times 10^{15}$ m^{-2}) and with an effective mass of $m_2 = (0.049 \pm 0.007)m_e$.

Extraction of the effective mass of the higher mobility carriers is independently corroborated by way of electron-cyclotron-resonance (CR) analysis under high magnetic field. Figure 5(a) displays the normalized transmission traces, T_B/T_0, at fixed magnetic fields ranging from 7 to 17 T, as a function of energy, demonstrating the evolution of the effective mass. Broad resonances are

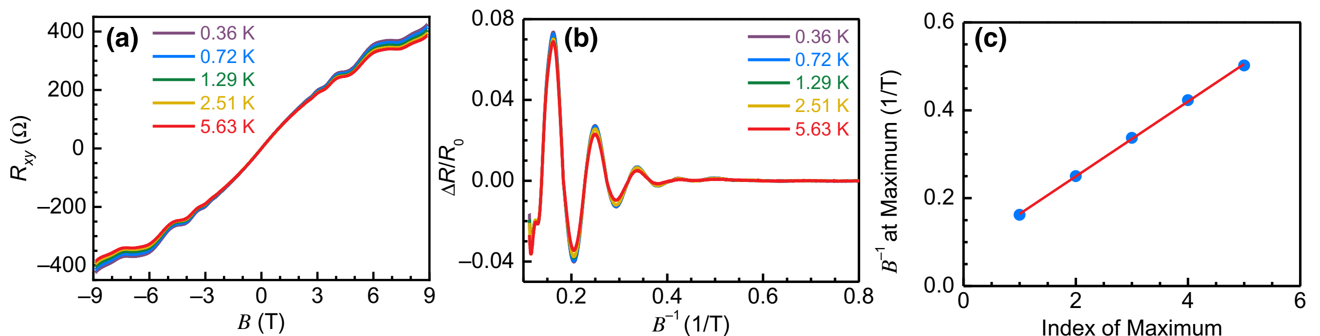

FIG. 4. (a) Transverse magnetoresistance (R_{xy} vs magnetic field, i.e., Hall effect) obtained in a van der Pauw configuration over temperatures 0.36 to 5.63 K and over magnetic fields ±9 T. Shubnikov-de Haas oscillations are visible at higher magnetic fields due to intermixing with longitudinal magnetoresistance. (b) Shubnikov-de Haas oscillations plotted versus inverse magnetic field. (c) Inverse magnetic field (symbols, blue) at the maxima in (b) versus the index of the maxima, with a linear fit (solid line, red) displaying slope $S = (0.0853 \pm 0.001)$ T^{-1}.

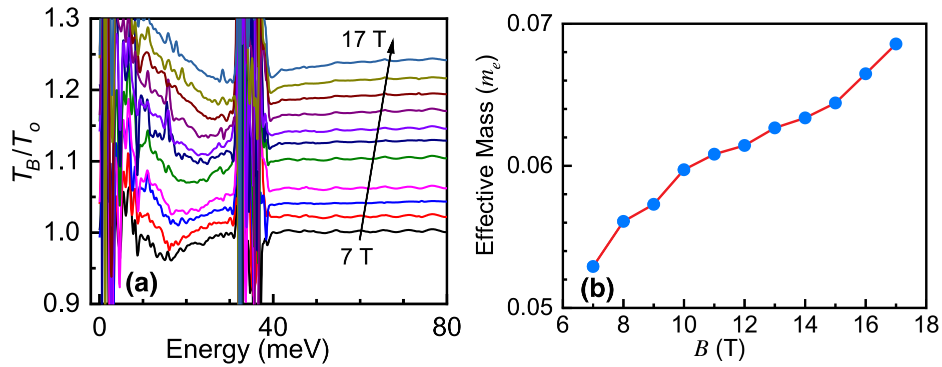

FIG. 5. (a) Normalized magnetotransmission traces, T_B/T_0, at fixed magnetic fields ranging from 7 to 17 T, as a function of energy; notably, traces are shifted for clarity. (b) Evolution of effective mass as a function of magnetic field, extracted from the resonance positions of the CR measurements, taken at 4.5 K (line is a guide for the eye).

observed as a result of the CR mobility of the carrier population being probed; however, extraction of the carrier effective mass as a function of the applied magnetic field, utilizing the measured resonance positions, is still possible, as shown in Fig. 5(b). The resulting effective mass at $B \approx 8$ T, $m^* = 0.056 m_e$, is found to be in good agreement with that determined *via* the temperature dependence of the Shubnikov-de Haas oscillations. The increase in m^* with increasing B is due to the nonparabolicity effect in the conduction band of ε-Ge. Similar observations

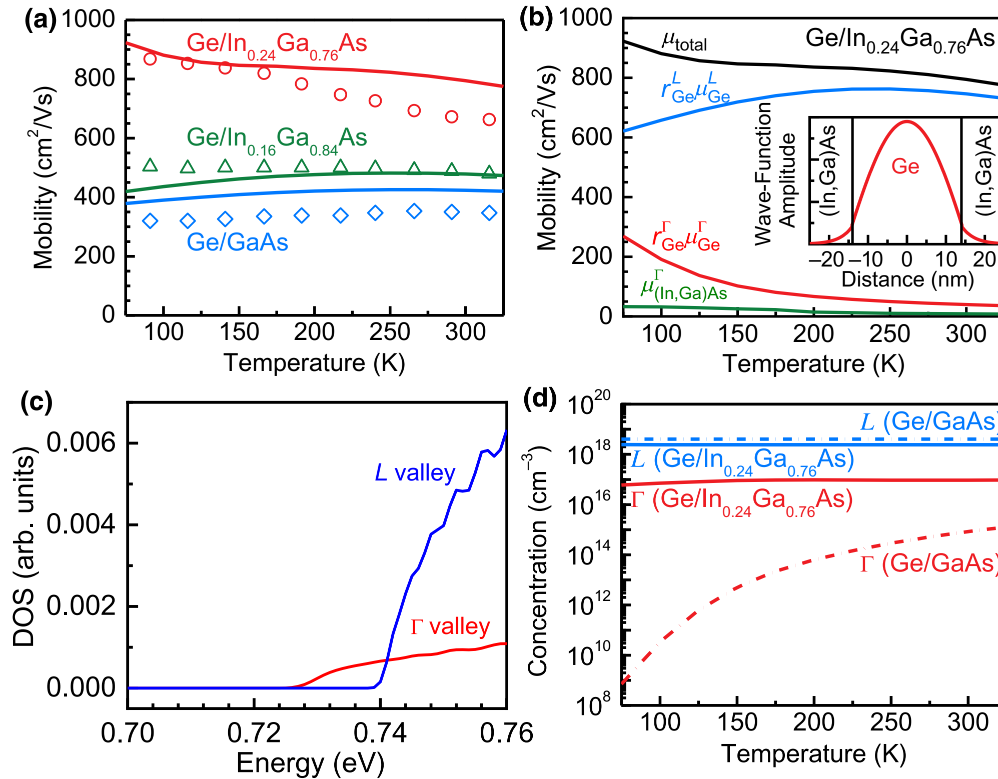

FIG. 6. (a) Measured (symbols) and calculated (solid lines) n-type mobility versus temperature in quantum-confined ε-Ge/In$_x$Ga$_{1-x}$As heterostructures for InAs mole fractions of 0, 0.16, and 0.24. Thicknesses of the Ge regions are (i) 80 nm, (ii) 15 nm, and (iii) 30 nm, for the 0, 0.16, and 0.24 In$_x$Ga$_{1-x}$As alloys, respectively [25]. (b) Temperature dependence of the calculated contributions to the total mobility from the L and Γ valleys in the ε-Ge region and the Γ valley in the In$_{0.24}$Ga$_{0.76}$As virtual substrate. Total mobility is given by $\mu_{\text{total}} = \sum_j r_j \mu_j$, where $r_j = n_j / n_{\text{total}}$ is the proportion of carriers in valley j. (c) DOS versus energy of L and Γ valleys, showing higher DOS in the L valley than in the Γ valley. (d) Temperature dependence of the calculated volumetric carrier concentrations in the L and Γ valleys of ε-Ge and the Γ valley of In$_{0.24}$Ga$_{0.76}$As for the 1.6% ε-Ge/In$_{0.24}$Ga$_{0.76}$As heterostructure.

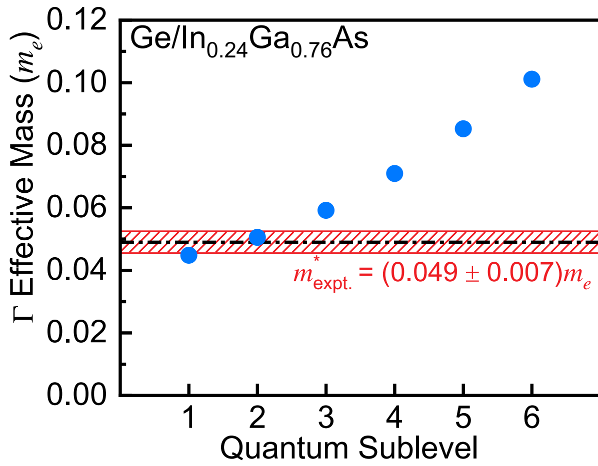

FIG. 7. Evolution of the ε-Ge Γ-valley effective mass with increasing quantum sublevel for the 1.6% ε-Ge/$In_{0.24}Ga_{0.76}As$ heterostructure at $T = 0$ K.

are reported in the literature for several material systems [64–71] due to nonparabolicity in the conduction band for n-type materials or in the valence band for p-type materials. However, neither measurement alone is sufficient to determine the carrier type of the higher mobility carriers. As such, electronic transport modeling of the ε-Ge/$In_xGa_{1-x}As$ material system is employed to provide additional insight into the empirical transport behavior.

C. Modeling of the strain-dependent electronic transport properties of Ge

To clarify the origin of the Shubnikov-de Haas oscillations and carrier effective mass previously probed, the mobility in several ε-Ge/$In_xGa_{1-x}As$ heterostructures is calculated using a parametrization of the Boltzmann transport equation based on first principles [20]. The temperature-dependent Hall mobility measurements of unstrained and tensile-strained Ge samples (see Table I) are performed using the van der Pauw geometry to determine the carrier density and mobility of each sample. Figure 6(a) shows the mobility calculated as a function of temperature for three different strain states, corresponding to Ge grown on GaAs, $In_{0.16}Ga_{0.84}As$, and $In_{0.24}Ga_{0.76}As$ alloys, as compared to experiments. The carrier densities for these layers are about 4×10^{18}, 7×10^{18}, and 2×10^{18} cm^{-3}, respectively. The symbols in this figure represent Hall mobiltiy data, and the calculated solid lines are fitted to experimental results. To fit the experimetal data of the Ge/AlAs sample (0% strain), a higher scattering rate for impurities is assumed since the measured mobility is quite low.

The n-type mobility ($N_e \approx 2 \times 10^{18}$ cm^{-3}) exhibits contributions from the L and Γ valleys in the ε-Ge region (1.6% ε-Ge/$In_{0.24}Ga_{0.76}As$), as well as the Γ valley in the $In_xGa_{1-x}As$ VS [Fig. 6(b)]; notably, the contribution from each valley is proportional to the amplitude of the wave function (of the corresponding valley) in each region. For biaxial tensile strains lower than 1.6%, all conduction is found to occur *via* the L valley in Ge. At strain states above 1.6%, the contribution from the Γ valley is found to increase, particularly at low (<150 K) temperatures. Figure 6(b) shows the contribution from each valley to the total mobility in the 1.6% ε-Ge/$In_{0.24}Ga_{0.76}As$ heterostructure. While transport primarily occurs *via* the L valley, at $T = 100$ K, the contribution of Γ-valley transport to the total mobility increases to 17%, diminishing with increasing temperature to approximately 3% at $T = 300$ K. These results can be explained by the much larger density of states within the L valley (i.e., the DOS masses of the L and Γ valleys are $m_L^{\mathrm{DOS}} = 0.22\ m_e$ and $m_\Gamma^{\mathrm{DOS}} = 0.05\ m_e$, respectively), which became increasingly populated with rising temperature. Figure 6(c) shows the calculated DOS versus energy in both L and Γ valleys under 1.6% tensile strain. One can find from this figure that the DOS in the Γ valley is lower than that of L valley and most of the carriers will still reside within the L valley. Additionally, in spite of the high electron mobility of the $In_{0.24}Ga_{0.76}As$ VS, it contributes comparatively little to the total mobility, owing to wave-function confinement within the ε-Ge region [Fig. 6(b), inset]. However, due to the smaller DOS of the Γ valley in Ge, such quantum confinement tends to decrease the mobility contribution of Γ-valley carriers to the total electron mobility, as compared to carriers residing in the higher DOS L valley in Ge. At room temperature, the carriers will populate both valleys, with more at the L valley than at the Γ valley due to higher DOS. The two ways one can increase the carrier density in the Γ valley are (i) by injecting carriers from the L valley by incorporating doping in the ε-Ge layer or (ii) during the lasing process by electrical injection [72].

Relating the transport modeling results to the aforementioned magnetotransport analysis, it is found that the measured electron population with a higher density ($N_{S1} = 8.50 \times 10^{16}$ m^{-2}) corresponds well to L-valley electron conduction in ε-Ge, whereas the lower population-density carriers ($N_{S2} = 5.67 \times 10^{15}$ m^{-2}), exhibiting an effective mass of $m_2 = (0.049 \pm 0.007)m_e$, represent Γ-valley electron conduction in ε-Ge. A comparison of the calculated carrier populations in the L and Γ valleys of Ge and $In_xGa_{1-x}As$ as a function of temperature [Fig. 6(d)] yield qualitative agreement with empirical magnetotransport data. Moreover, calculation of the Γ-valley transport effective mass in 1.6% ε-Ge (Fig. 7) reveals excellent agreement between the effective masses of the first-two quantum sublevels ($0.045m_e$ and $0.051m_e$, respectively) and that measured by experiments. As such, it can thus be posited that the effective mass of the relatively higher mobility carriers probed *via* the magnetotransport and CR studies corresponds to electrons residing in the first-two energy levels of the Γ valley in ε-Ge. Taken as a whole,

however, these results indicate that $\varepsilon > 1.6\%$ is likely to be necessary to increase Γ-valley occupancy and, therefore, enhance the Γ-valley contribution to the total ε-Ge mobility.

IV. CONCLUSIONS

We provide a fundamental insight into the nature of electronic transport in highly tensile-strained Ge materials, along with their detailed structural analysis by x-ray, Raman, and cross-section and plan-view transmission electron microscopy. The quantification of defects and surface roughness are provided in the Supplemental Material [46]. The presented magnetotransport and cyclotron-resonance results, when coupled with our first-principles-parameterized Boltzmann transport modeling, reveal the strain dependence of L- and Γ-valley conduction in tensile-strained Ge. The temperature dependence of the calculated mobility and carrier contributions in each valley of 1.6% ε-Ge are decoupled based on the experimental Hall measurement results, and most of the carriers will reside within the L valley due to a higher density of states. In addition, the effective mass, $m^* \approx 0.056 m_e$, determined *via* cyclotron resonance is in agreement with Shubnikov-de Haas oscillations. Moreover, the temperature-dependent competitiveness between L- and Γ-valley conduction in tensile-strained Ge has significant importance for future electron devices, such as strained Ge-based gate-all-around nanowire FETs [13,15] and tunnel FETs [19,24], wherein epitaxial strain is a key mechanism for improving carrier mobility and a device's drive current. Our results, however, are not limited to Ge-based electronics, as we also demonstrate direct experimental probing of the electron effective mass in Ge under high strain, thereby allowing for comparison with current and previous theoretical results [11,17–19].

ACKNOWLEDGMENTS

M.C. acknowledges financial support from the NSF under Grant No. ECCS-1348653. M.H. acknowledges partial support from the NSF under Grant No. ECCS-ECCS-2042079, a US-Ireland joint R&D program. G.A.K. acknowledges support from the Air Force Office of Scientific Research under Grant No. FA9550-17-1-0341. F. M. A. acknowledges financial support from Science Foundation Ireland Frontiers of the Future Program SFI/19/FFP/6953 and the US-Ireland R&D Partnership Program by Science Foundation Ireland (SFI) Grants No. SFI/20/US/3692 and SFI/14/US/I3057. The authors also acknowledge the NCFL Institute for Critical Technology and Applied Science and Virginia Tech Nanofabrication for providing material characterization facilities. M.C. and M.H. would also like to acknowledge Dr. Patrick Goley for assisting with the TEM imaging. Lastly, a portion of this work is performed at the National High Magnetic Field Laboratory, which is supported by the National Science Foundation Cooperative Agreement No. DMR-1157490 and the State of Florida.

[1] T. Ghani, M. Armstrong, C. Auth, M. Bost, P. Charvat, G. Glass, T. Hoffmann, K. Johnson, C. Kenyon, J. Klaus, *et al.*, A 90 nm high volume manufacturing logic technology featuring novel 45 nm gate length strained silicon CMOS transistors, IEEE Int. Electron Devices Meet. (IEDM), 11.6.1 (2003).

[2] C.-H. Ge, C.-C. Lin, C.-H. Ko, C.-C. Huang, Y.-C. Huang, B.-W. Chan, B.-C. Pemg, C.-C. Sheu, P.-Y. Tsai, L.-G. Yao, *et al.*, Process-strained Si (PSS) CMOS technology featuring 3D strain engineering, IEEE Int. Electron Devices Meet. (IEDM), 3.7.1 (2003).

[3] S. E. Thompson, M. Armstrong, C. Auth, M. Alavi, M. Buehler, R. Chau, S. Cea, T. Ghani, G. Glass, T. Hoffman, *et al.*, A 90-nm logic technology featuring strained-silicon, IEEE Trans. Electron Devices **51**, 1790 (2004).

[4] Q. Ouyang, M. Yang, J. Holt, S. Panda, H. Chen, H. Utomo, M. Fischetti, N. Rovedo, J. Li, N. Klymko, *et al.*, Investigation of CMOS devices with embedded SiGe source/drain on hybrid orientation substrates, Symp. VLSI Technol. Tech. Dig., 28 (2005).

[5] D. K. Nayak, K. Goto, A. Yutani, J. Murota, and Y. Shiraki, High-mobility strained-Si PMOSFET's, IEEE Trans. Electron Devices **43**, 1709 (1996).

[6] R. Chau, B. Doyle, S. Datta, J. Kavalieros, and K. Zhang, Integrated nanoelectronics for the future, Nat. Mater. **6**, 810 (2007).

[7] R. Pillarisetty, Academic and industry research progress in germanium nanodevices, Nature **479**, 324 (2011).

[8] M. Heyns, A. Alian, G. Brammertz, M. Caymax, Y. C. Chang, L. K. Chu, B. De Jaeger, G. Eneman, F. Gencarelli, G. Groeseneken, *et al.*, Advancing CMOS beyond the Si roadmap with Ge and III/V devices, IEEE Int. Electron Devices Meet. (IEDM), 13.1.1 (2011).

[9] K. J. Kuhn, Considerations for ultimate CMOS scaling, IEEE Trans. Electron Devices **59**, 1813 (2012).

[10] P. D. Nguyen, M. B. Clavel, P. S. Goley, J.-S. Liu, N. P. Allen, L. J. Guido, and M. K. Hudait, Heteroepitaxial Ge MOS devices on Si using composite AlAs/GaAs buffer, IEEE J. Electron Devices Soc. **3**, 341 (2015).

[11] M. V. Fischetti and S. E. Laux, Band structure, deformation potentials, and carrier mobility in strained Si, Ge, and SiGe alloys, J. Appl. Phys. **80**, 2234 (1996).

[12] J. Kim and M. V. Fischetti, Electronic band structure calculations for biaxially strained Si, Ge, and III–V semiconductors, J. Appl. Phys. **108**, 013710 (2010).

[13] W. Chern, P. Hashemi, J. T. Teherani, T. Yu, Y. Dong, G. Xia, D. A. Antoniadis, and J. L. Hoyt, High mobility high-κ-all-around asymmetrically strained germanium nanowire trigate p-MOSFETs, IEEE Int. Electron Devices Meet. (IEDM), 16.5.1 (2012).

[14] A. Agrawal, M. Barth, G. B. Rayner, V. T. Arun, C. Eichfeld, G. Lavallee, S.-Y. Yu, X. Sang, S. Brookes, Y. Zheng, *et al.*, Enhancement mode strained (1.3%) germanium

quantum well FinFET ($W_{\mathrm{Fin}} = 20$ nm) with high mobility ($\mu_{\mathrm{Hole}} = 700$ cm^2/Vs), low EOT (~0.7 nm) on bulk silicon substrate, IEEE Int. Electron Devices Meet. (IEDM), 16.4.1 (2014).

[15] L. Witters, H. Arimura, F. Sebaai, A. Hikavyy, A. P. Milenin, R. Loo, A. De Keersgieter, G. Eneman, T. Schram, K. Wostyn, *et al.*, Strained germanium gate-all-around pMOS device demonstration using selective wire release etch prior to replacement metal gate deposition, IEEE Trans. Electron Devices **64**, 4587 (2017).

[16] K. Wang, Q. Gong, H. Zhou, C. Kang, J. Yan, Q. Liu, and S. Wang, Mobility enhancement in tensile-strained Ge grown on InAlP metamorphic templates, Appl. Surf. Sci. **291**, 45 (2014).

[17] D. Rideau, M. Feraille, L. Ciampolini, M. Minondo, C. Tavernier, H. Jaouen, and A. Ghetti, Strained Si, Ge, and $Si_{1-x}Ge_x$ alloys modeled with a first-principles-optimized full-zone **k·p** method, Phys. Rev. B **74**, 195208 (2006).

[18] M. El Kurdi, G. Fishman, S. Sauvage, and P. Boucaud, Band structure and optical gain of tensile-strained germanium based on a 30 band **k·p** formalism, J. Appl. Phys. **107**, 013710 (2010).

[19] K.-H. Kao, A. S. Verhulst, M. Van de Put, W. G. Vandenberghe, B. Soree, W. Magnus, and K. De Meyer, Tensile strained Ge tunnel field-effect transistors: **k·p** material modeling and numerical device simulation, J. Appl. Phys. **115**, 044505 (2014).

[20] F. Murphy-Armando and S. Fahy, Giant enhancement of *n*-type carrier mobility in highly strained germanium nanostructures, J. Appl. Phys. **109**, 113703 (2011).

[21] M. K. Hudait, F. Murphy-Armando, D. Saladukha, M. B. Clavel, P. S. Goley, D. Maurya, S. Bhattacharya, and T. J. Ochalski, Design, theoretical and experimental investigation of tensile-strained germanium quantum-well laser structure, ACS Appl. Electron. Mater. **10**, 4535 (2021).

[22] D. Saladukha, M. B. Clavel, F. Murphy-Armando, G. Greene-Diniz, M. Gruening, M. K. Hudait, and T. J. Ochalski, Direct and indirect band gaps in Ge under biaxial tensile strain investigated by photoluminescence and photoreflectance studies, Phys. Rev. B **97**, 195304 (2018).

[23] M. K. Hudait, M. Clavel, L. Lester, D. Saladukha, T. Ochalski, and F. Murphy-Armando, in *Proc. SPIE 9755, Quantum Sensing and Nano Electronics and Photonics XIII, 97550Y* (February 13, 2016).

[24] J.-S. Liu; M, B. Clavel, and M. K. Hudait, Performance evaluation of novel strain-engineered Ge-InGaAs heterojunction tunnel field-effect transistors, IEEE Trans. Electron Devices **62**, 3223 (2015).

[25] M. Clavel, P. Goley, N. Jain, Y. Zhu, and M. K. Hudait, Strain-engineered biaxial tensile epitaxial germanium for high-performance Ge/InGaAs tunnel field-effect transistors, IEEE J. Electron Dev. Soc. **3**, 184 (2015).

[26] J.-S. Liu, M. Clavel, and M. K. Hudait, An energy-efficient tensile-strained Ge/InGaAs TFET 7T SRAM cell architecture for ultra-low voltage applications, IEEE Trans. Electron Devices **64**, 2193 (2017).

[27] J.-S. Liu, M. Clavel, and M. K. Hudait, TBAL: Tunnel FET-based adiabatic logic for energy-efficient, ultra-low voltage IoT applications, IEEE J. Electron Dev. Soc. **7**, 210 (2019).

[28] S. Bao, D. Kim, C. Onwukaeme, S. K. Gupta, K. Saraswat, K. H. Lee, Y. Kim, D. Min, Y. Jung, H. Qiu, *et al.*, Low-threshold optically pumped lasing in highly strained germanium nanowires, Nature Communication **8**, 1845 (2017).

[29] S. Gupta, D. Nam, J. Vuckovic, and K. Saraswat, Room temperature lasing unraveled by a strong resonance between gain and parasitic absorption in uniaxially strained germanium, Phys. Rev. B **97**, 155127 (2018).

[30] J. Petykiewicz, D. Nam, D. S. Sukhdeo, S. Gupta, S. Buckley, A. Y. Piggott, J. Vučković, and K. C. Saraswat, Direct bandgap light emission from strained germanium nanowires coupled with high-*Q* nanophotonic cavities, Nano Lett. **16**, 2168 (2016).

[31] C. Morrison and M. Myronov, Strained germanium for applications in spintronics, Phys. Status Solidi A **213**, 2809 (2016).

[32] L. A. Terrazos, E. Marcellina, Z. Wang, S. N. Coppersmith, M. Friesen, A. R. Hamilton, X. Hu, B. Koiller, A. L. Saraiva, D. Culcer, *et al.*, Theory of hole-spin qubits in strained germanium quantum dots, Phys. Rev. B **103**, 12 (2021).

[33] A. Sammak, D. Sabbagh, N. W. Hendrickx, M. Lodari, B. P. Wuetz, A. Tosato, L. Yeoh, M. Bollani, M. Virgilio, M. A. Schubert, *et al.*, Shallow and undoped germanium quantum wells: A playground for spin and hybrid quantum technology, Adv. Functional Materials **29**, 1807613 (2019).

[34] Y. Bai, K. E. Lee, C. Cheng, M. L. Lee, and E. A. Fitzgerald, Growth of highly tensile-strained Ge on relaxed $In_xGa_{1-x}As$ by metal-organic chemical vapor deposition, J. Appl. Phys. **104**, 084518 (2008).

[35] R. Jakomin, M. de Kersauson, M. El Kurdi, L. Largeau, O. Mauguin, G. Beaudoin, S. Sauvage, R. Ossikovski, G. Ndong, M. Chaigneau, *et al.*, High quality tensile-strained *n*-doped germanium thin films grown on InGaAs buffer layers by metal-organic chemical vapor deposition, Appl. Phys. Lett. **98**, 091901 (2011).

[36] F. Murphy-Armando and S. Fahy, First-principles calculation of carrier-phonon scattering in *n*-type $Si_{1-x}Ge_x$ alloys, Phys. Rev. B **78**, 035202 (2008).

[37] F. Murphy-Armando, Enhancement of the electronic thermoelectric properties of bulk strained silicon-germanium alloys using the scattering relaxation times from first-principles calculations, J. Appl. Phys. **126**, 215103 (2019).

[38] C. Jacoboni and L. Reggiani, The Monte Carlo method for the solution of charge transport in semiconductors with applications to covalent materials, Rev. Mod. Phys. **55**, 645 (1983).

[39] D. Chattopadhyay and H. Queisser, Electron scattering by ionized impurities in semiconductors, Rev. Mod. Phys. **53**, 745 (1981).

[40] R. Barrie, Electronic conduction in solids with spherically symmetric band structure, Proc. Phys. Soc. B **69**, 553 (1956).

[41] Y. A. Goldberg and N. M. Schmidt, *Handbook Series on Semiconductor Parameters* (World Scientific, London, 1999), Vol. II, pp. 62–88.

[42] N. Pavarelli, T. J. Ochalski, F. Murphy-Armando, Y. Huo, M. Schmidt, G. Huyet, and J. S. Harris, Optical Emission of a Strained Direct-Band-Gap Ge Quantum Well Embedded

Inside InGaAs Alloy Layers, Phys. Rev. Lett. **110**, 177404 (2013).

[43] J.-M. Chauveau, Y. Androussi, A. Lefebvre, J. Di Persio, and Y. Cordier, Indium content measurements in metamorphic high electron mobility transistor structures by combination of x-ray reciprocal space mapping and transmission electron microscopy, J. Appl. Phys. **93**, 4219 (2003).

[44] M. K. Hudait, Y. Lin, and S. A. Ringel, Strain relaxation properties of InAsyP1$_{-}y$ metamorphic materials grown on InP substrates, J. Appl. Phys. **105**, 061643 (2009).

[45] R. S. Goldman, H. H. Wieder, and K. L. Kavanagh, Correlation of anisotropic strain relaxation with substrate misorientation direction at InGaAs/GaAs(001) interfaces, Appl. Phys. Lett. **67**, 344 (1995).

[46] See the Supplemental Material at http://link.aps.org/supplemental/10.1103/PhysRevApplied.18.064083 for extended discussions of the ε-Ge/$In_{0.24}Ga_{0.76}As$ heterostructure's surface morphological properties, Raman spectroscopy analysis methodology, and TEM dislocation-identification methodology.

[47] A. M. Andrews, A. E. Romanov, J. S. Speck, M. Bobeth, and W. Pompe, Development of cross-hatch morphology during growth of lattice mismatched layers, Appl. Phys. Lett. **77**, 3740 (2000).

[48] A. M. Andrews, J. S. Speck, A. E. Romanov, M. Bobeth, and W. Pompe, Modeling cross-hatch surface morphology in growing mismatched layers, J. Appl. Phys. **91**, 1933 (2002).

[49] M. Natali, F. Romanato, E. Napolitani, D. De Salvador, and A. V. Drigo, Lattice curvature generation in graded $In_xGa_{1-x}As$/GaAs buffer layers, Phys. Rev. B **62**, 11054 (2000).

[50] M. B. Clavel and M. K. Hudait, Band offset enhancement of a-Al_2O_3/tensile-Ge for high mobility nanoscale pMOS devices, IEEE Electron Device Lett. **38**, 1196 (2017).

[51] E. Anastassakis and M. Cardona, *High Pressure in Semiconductor Physics II* (Academic Press, San Diego, 1998), Vol. 55, Chap. 3.

[52] Z. Sui and I. P. Herman, Effect of strain on phonons in Si, Ge, and Si/Ge heterostructures, Phys. Rev. B **48**, 17938 (1993).

[53] M. Clavel, D. Saladukha, P. S. Goley, T. J. Ochalski, F. Murphy-Armando, R. J. Bodnar, and M. K. Hudait, Heterogeneously-grown tunable tensile strained germanium on silicon for photonic devices, ACS Appl. Mater. Interfaces **7**, 26470 (2015).

[54] O. Madelung, *Semiconductors: Intrinsic Properties of Group IV Elements and III-V, II-VI, and I-VII Compounds* (Springer, Berlin, 1985), Vol. 22a.

[55] Y.-Y. Fang, J. Tolle, R. Roucka, A. V. G. Chizmeshya, J. Kouvetakisa, V. R. D'Costa, and J. Menéndez, Perfectly tetragonal, tensile-strained Ge on $Ge_{1-y}Sn_y$ buffered Si(100), Appl. Phys. Lett. **90**, 061915 (2007).

[56] J. Petruzzello and M. R. Leys, Effect of the sign of misfit strain on the dislocation structure at interfaces of heteroepitaxial $GaAs_xP_{1-x}$ films, Appl. Phys. Lett. **53**, 2414 (1988).

[57] J. Ayers, *Heteroepitaxy of Semiconductors: Theory, Growth, and Characterization* (CRC Press, Boca Raton, 2007), pp. 36–67. Chap. 5.

[58] A. F. Marshall, D. B. Aubertine, W. D. Nix, and P. C. McIntyre, Misfit dislocation dissociation and Lomer formation in low mismatch SiGe/Si heterostructures, J. Mater. Res. **20**, 447 (2005).

[59] H. Gottschalk, Motion of partial dislocations, J. Phys. Colloques **40**, 127 (1979).

[60] N. A. El-Masry, J. C. Tarn, and N. H. Karam, Interactions of dislocations in GaAs grown on Si substrates with InGaAs-GaAsP strained layer superlattices, J. Appl. Phys. **64**, 3672 (1988).

[61] C. Morrison and M. Myronov, Electronic transport anisotropy of 2D carriers in biaxial compressive strained germanium, Appl. Phys. Lett. **111**, 192103 (2017).

[62] R. Pisoni, A. Kormányos, M. Brooks, Z. Lei, P. Back, M. Eich, H. Overweg, Y. Lee, P. Rickhaus, K. Watanabe, *et al.*, Interactions and Magnetotransport through Spin-valley Coupled Landau Levels in Monolayer MoS_2, Phys. Rev. Lett. **121**, 247701 (2018).

[63] P. T. Coleridge, Small-angle scattering in two-dimensional electron gases, Phys. Rev. B **44**, 3793 (1991).

[64] M. J. Yang, P. J. Lin-Chung, R. J. Wagner, J. R. Waterman, W. J. Moore, and B. V. Shanabrook, Far-infrared spectroscopy in strained AlSb/InAs/AlSb quantum wells, Semicond. Sci. Technol. **8**, S129 (1993).

[65] V. Y. Aleshkin, V. I. Gavrilenko, A. V. Ikonnikov, Y. G. Sadofyev, J. P. Bird, S. R. Johnson, and Y.-H. Zhang, Cyclotron resonance in doped and undoped InAs/AlSb heterostructures with quantum wells, Semiconductors **39**, 62 (2005).

[66] T. E. Whall, A. D. Plews, N. L. Mattey, P. J. Phillips, and U. Ekenberg, Effective mass and band nonparabolicity in remote doped $Si/Si_{0.8}Ge_{0.2}$ quantum wells, Appl. Phys. Lett. **66**, 2724 (1995).

[67] G. C. Osbourn, J. E. Schirber, T. J. Drummond, L. R. Dawson, B. L. Doyle, and I. J. Fritz, Large valence-band nonparabolicity and tailorable hole masses in strained-layer superlattices, Appl. Phys. Lett. **49**, 731 (1986).

[68] O. Drachenko, D. V. Kozlov, V. Y. Aleshkin, V. I. Gavrilenko, K. V. Maremyanin, A. V. Ikonnikov, B. N. Zvonkov, M. Goiran, J. Leotin, G. Fasching, *et al.*, High-field splitting of the cyclotron resonance absorption in strained p-InGaAs/GaAs quantum wells, Phys. Rev. B **79**, 073301 (2009).

[69] J. E. Schirber, I. J. Fritz, and L. R. Dawson, Light-hole conduction in InGaAs/GaAs strained-layer superlattices, Appl. Phys. Lett. **46**, 187 (1985).

[70] N. Tang, B. Shen, M. J. Wang, Z. J. Yang, K. Xu, G. Y. Zhang, T. Lin, B. Zhu, W. Z. Zhou, and J. H. Chu, Influence of the magnetic field on the effective mass of the two-dimensional electron gas in $Al_xGa_{1-x}N$/GaN heterostructures, Phys. Status Solidi C **3**, 2246-2249 (2006).

[71] Y. H. Park, H. C. Koo, K. H. Kim, H. Kim, J. Chang, and S. H. Han, Influence of the magnetic field on the effective mass and the Rashba effect in an $In_{0.53}Ga_{0.47}As$ quantum-well structure, J. Korean Phys. Soc. **57**, 1929 (2010).

[72] *Photonics and Electronics with Germanium*, edited by K. Wada and L. C. Kimerling (Wiley-VCH, Weinheim, Germany, 2015), Chap. 12, pp. 267–303.

Supplemental Material: Multi-Valley Electron Conduction at the Indirect-Direct Crossover Point in Highly-Tensile-Strained Germanium

M. B. Clavel[1], F. Murphy-Armando[2], Y. Xie[3], K. T. Henry[4], M. Kuhn[4], R. J. Bodnar[5], G. A. Khodaparast[3], D. Smirnov[6], J. J Heremans[3], and M. K. Hudait[1*]

[1]*Advanced Devices & Sustainable Energy Laboratory (ADSEL), Bradley Department of Electrical and Computer Engineering, Virginia Tech, Blacksburg, Virginia 24061, USA*
[2]*Tyndall National Institute, University College Cork, Lee Maltings, Dyke Parade, Cork, Ireland*
[3]*Department of Physics, Virginia Tech, Blacksburg, Virginia 24061, USA*
[4]*Intel Corporation, Hillsboro, Oregon, USA*
[5]*Fluids Research Laboratory, Department of Geosciences, Virginia Tech, Blacksburg, Virginia 24061, USA*
[6]*National High Magnetic Field Laboratory, Tallahassee, Florida 32310, USA*

I. ε-Ge/$In_{0.24}Ga_{0.76}As$ Heterostructure Surface Morphology

Surface morphology characterization *via* atomic force microscopy (AFM) provides an additional means of investigating the strain relaxation dynamics of metamorphic heterostructures. In particular, the strain relief mechanisms that govern film relaxation during the growth of mismatched (001) oriented cubic materials are known to result in cross-hatch surface patterns wherein surface topography can be directly correlated with the nature and degree of strain relaxation within the film(s) [47,48]. This cross-hatch morphology originates from plastic relaxation processes as film thickness exceeds the critical thickness for the release of accumulated strain energy. Within this regime, initial misfit stress is relaxed by threading dislocation (TD) formation and glide, thereby creating slip steps at the film surface and misfit dislocations (MDs) at the film/substrate interface. For (001) oriented cubic systems, the most common slip system is $a/2\ \langle 110\rangle\{111\}$, indicating that the TDs and associated MDs that form occur within $\{111\}$ planes (α ≈ 54.7°) and propagate laterally along $\langle 110\rangle$ directions [49]. The step formation that occurs at the growth front is subsequently smoothed *via* lateral mass transport and preferential step-site growth, *i.e.*, in a typical step-flow growth process. Successive relaxation results in the formation of hillocks and valleys oriented along dislocation lines and in the vicinity of buried MDs. Hence, any anisotropy in relaxation along orthogonal $\langle 110\rangle$ directions can be directly evidenced by an asymmetry in the ultimate cross-hatch topography. In the case of lattice-mismatched $In_xGa_{1-x}As$ on GaAs epitaxy, an additional source of anisotropic strain relaxation is due to the disparity between α (As-terminated core) and β (Ga-terminated core) dislocation glide velocities oriented along the $[1\bar{1}0]$ and $[110]$ directions, respectively [49]. Thus, for a metamorphic $In_xGa_{1-x}As$ film with isotropic strain relaxation, it would be expected that the surface exhibit a symmetric cross-hatch pattern with peak-to-valley amplitude and uniformity dependent on film thickness and the degree of relaxation [47–49]. A minor degree of asymmetry between the $[1\bar{1}0]$ and $[110]$ oriented surface features could arise due to the associated difference in dislocation glide velocities; however, a large asymmetry in the cross-hatch morphology would suggest a strong degree of anisotropic strain relaxation and the presence of epitaxial tilt or similar defect-related film non-idealities.

As can be seen from Fig. S1, a representative 20 µm × 20 µm AFM micrograph of the ε-Ge/$In_{0.24}Ga_{0.76}As$ heterostructure's surface reveals a distinct, symmetric cross-hatch with a peak-to-valley amplitude of ~9 nm and RMS roughness (R_q) of 3.35 nm. The degree of uniformity between the orthogonal $[1\bar{1}0]$ and $[110]$ directions is indicative of a largely isotropic film relaxation. Nevertheless, the $[1\bar{1}0]$ oriented surface features exhibit a qualitatively coarser topography. Quantitative analysis of

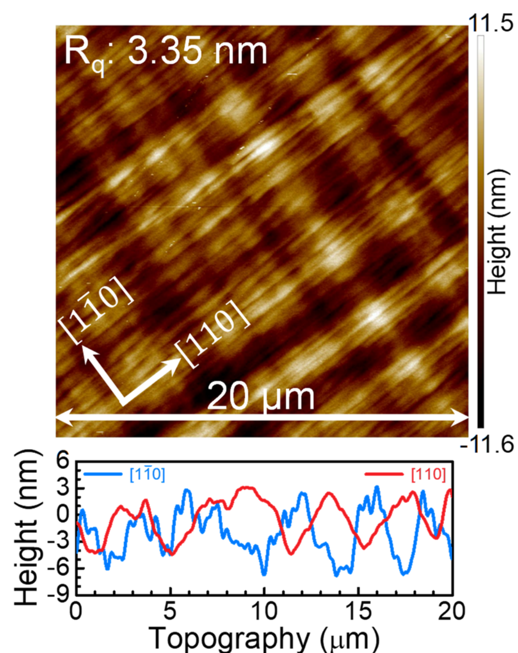

FIG. S1. Atomic force micrograph of a representative 20 µm × 20 µm region of the as-grown ε-Ge/$In_{0.24}Ga_{0.76}As$ surface and associated line height profiles taken along the two orthogonal $\langle 110\rangle$ symmetric directions.

line height profiles taken along the $[1\bar{1}0]$ and $[110]$ directions yield different R_q values, *i.e.*, 3.28 nm and 2.24 nm, respectively, suggesting a greater degree of relaxation in the $[110]$ direction. This is reinforced by the comparatively larger separation between hillocks and valleys in the $[110]$ line profile, which has been previously correlated to a high degree of relaxation in thick (~1 μm) $In_{0.25}Ga_{0.75}As$ films grown on GaAs [48]. Moreover, the slight asymmetry observed in our AFM findings corresponds well to the observed tilt (~540 arcsec) measured *via* XRD, indicating a small but measurable degree of anisotropy in buffer strain relaxation during growth. We attribute this anisotropy to the previously discussed difference in dislocation velocities for α ($[1\bar{1}0]$ oriented) and β ($[110]$ oriented) dislocations.

II. Supplementary Methods 1: Raman Spectroscopy

For (001) oriented diamond-cubic crystals, the effect of biaxial strain is to split the threefold degenerate zone-center optical phonon modes into a doublet and singlet having eigenvectors perpendicular and parallel to the plane, respectively [51,52]. Thus, following the selection rules provided in Ref. [51,52], only the longitudinal optical (LO) mode corresponding to the singlet is observable under the (001) backscattering geometry utilized in this work. Moreover, the incorporation of lattice strain results in a hydrostatic shift of the phonon frequency (Ω_s) and thus a relative shift in the measured Raman wavenumber ($\Delta\omega$) with respect to its unstrained value (ω_0). The magnitude and sign of the resultant wavenumber shift is indicative of the material's strain-state and type of strain present within the system, *i.e.*, a positive or negative $\Delta\omega$ corresponds to compressive or tensile strain, respectively. In our previous work [53], we have used the relation $\Delta\omega = -b\varepsilon_{||}$ cm^{-1} to analyze the Raman shift as a function of strain ($\varepsilon_{||}$) for moderately strained ε-Ge epilayers grown on $In_xGa_{1-x}As$ metamorphic stressors heterogeneously integrated onto Si substrates. In the preceding expression, $\Delta\omega$ is the measured wavenumber shift (in cm^{-1}) whereas b can be expressed as [51,52]:

$$b = \omega_0\left(\widetilde{K}_{11}\frac{C_{12}}{C_{11}} - \widetilde{K}_{12}\right), \quad \text{(S1)}$$

where $\widetilde{K}_{11}$ and $\widetilde{K}_{12}$ are the phonon deformation potentials normalized to ω_0^2, ω_0 is the unstrained phonon frequency (~300 cm^{-1} for Ge), and C_{11} and C_{12} are material elastic constants. We note that the expression for $\Delta\omega$ assumes an isotropic, tetragonal strain of the form:

$$\varepsilon = \begin{pmatrix} \varepsilon_{||} & 0 & 0 \\ 0 & \varepsilon_{||} & 0 \\ 0 & 0 & \varepsilon_{\perp} \end{pmatrix}, \quad \text{(S2)}$$

in order to simplify the phonon secular equation and derive the expression for the strain-modified phonon frequency and hence the relative shift, $\Delta\omega$, in phonon frequency as a function of strain. Using the above expression and the material parameters found in Ref. [51,54], b was calculated to be -415 cm^{-1} [34,55].

III. Supplementary Methods 2: TEM Dislocation Identification

As previously discussed with respect to the investigated AFM surface morphology, dislocation formation occurs during the heteroepitaxy of metamorphic thin films in order to relieve accumulated lattice mismatch-induced film stress. Due to the packing density of $\{111\}$ atomic planes in (001)-oriented diamond cubic and zinc-blende crystals, such planes preferentially exhibit lattice distortions due to relaxation processes during growth [57]. The nucleation of dislocation half-loops at the film surface and their subsequent glide, both toward the lattice mismatched heterointerface (following $\{111\}$ slip planes) and the substrate edge (along $\langle 110\rangle$ directions) [49], is known to result in several dislocation structures, including, but not limited to: (i) threading dislocations (TDs) propagating along the growth direction; (ii) misfit dislocations (MDs) observed at the lattice-mismatched heterointerface; and (iii), stacking faults (SFs), originating from the dissociation of perfect 60° MDs into 90° and 30° Shockley partial dislocations [56–59]. These dislocations represent localized lattice disorder, and as such, also introduce local strain gradients surrounding the dislocation core, which can be utilized in practice in order to identify, *e.g.*, TDs at a film's surface. Figure S2(a) presents a representative plan-view TEM (PV-TEM) micrograph of the ε-Ge/$In_{0.24}Ga_{0.76}As$ heterostructure, wherein the top ~30 nm of ε-Ge has been etched in order to expose the underlying TDs propagating through the $In_{0.24}Ga_{0.76}As$ stressor. The diffraction contrast induced by the interaction between the diffracted electrons and the strain gradient surrounding the TDs is evident, as highlighted in Fig. S2(a). Using the diffraction contrast in order to identify TDs at the $In_{0.24}Ga_{0.76}As$ surface (*i.e.*, the ε-Ge/ $In_{0.24}Ga_{0.76}As$ interface of the as-grown heterostructure), a conservative estimate for the TD areal density, ρ_{TDD}, was found to be $\leq 2\times10^7$ cm^{-2}.

Similarly, MDs in the vicinity of the lattice-mismatched heterointerface are identifiable as disruptions to the otherwise ordered atomic planes when examined under cross-section using high magnification. Fig. S2(b) presents the origin of such MDs for the $\{111\}$ slip system, wherein $\boldsymbol{u}$ represents the dislocation line, $\boldsymbol{\tau}$ the resolved shear stress on the planes, and $\boldsymbol{b}$, $\boldsymbol{b_1}$, and $\boldsymbol{b_2}$ are the Burgers vectors for the 60° perfect, 90° partial, and 30° partial dislocations, respectively [56]. For tensile interfaces, it is energetically favorable for the 60° perfect dislocation to dissociate, first nucleating the 90° partial dislocation and giving rise to a stacking fault [56,58,59]. Assuming a dislocation line parallel to the $[1\bar{1}0]$ direction, the Burgers vector for the 90° and 30° partial dislocations could be given by $a/6\,[112]$ and $a/6\,[211]$, respectively. Should dislocation glide continue,

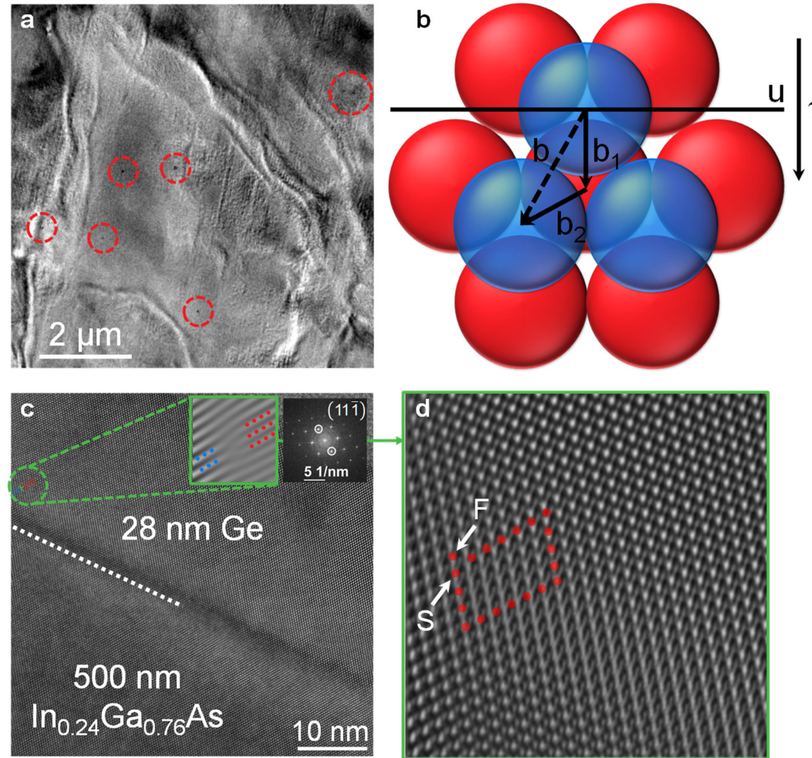

FIG. S2. (a) Plan-view TEM micrograph of the ε-Ge/$In_{0.24}Ga_{0.76}As$ heterostructure wherein the top 30 nm ε-Ge epilayer has been etched in order to identify threading dislocations in the underlying $In_{0.24}Ga_{0.76}As$ stressor. (b) Schematic representation of the Burgers vectors for leading 90° partial, trailing 30° partial, and perfect 60° dislocations – $\boldsymbol{b_1}$, $\boldsymbol{b_2}$, and $\boldsymbol{b}$, respectively – originating in {111} planes within a semiconductor having a diamond cubic (or zinc-blende) crystal structure. Adapted from Petruzzello *et al.* [56]. (c) Representative misfit dislocation in the ε-Ge epilayer, identified as originating in the $(11\bar{1})$ plane, and (d) its associated Burgers circuit.

the 30° partial dislocation will subsequently nucleate, reacting with the 90° partial dislocation following [57]:

$$\frac{a}{6}[112] + \frac{a}{6}[211] \rightarrow \frac{a}{2}[101]. \tag{S3}$$

The result of this reaction is the annihilation of the stacking fault and the formation of a perfect 60° dislocation. Thus, the type of lattice disorder introduced *via* MD formation can be used to identify the corresponding MD. Figs. S2(c) and S2(d) present a representative high-magnification cross-sectional TEM micrograph, from which the $(11\bar{1})$ plane was used (Fig. S2(c), insets) to identify MDs in the vicinity of the ε-Ge/$In_{0.24}Ga_{0.76}As$ heterointerface, and the corresponding Burgers circuit tracing the lattice distortion surrounding a representative MD, respectively. As can be seen from Fig. S2(c), the MD was associated with the insertion of an additional atomic plane (*i.e.*, an edge dislocation having a dislocation line within the plane of the page). Moreover, examination of the Burgers circuit encompassing the MD (Fig. S2(d)) reveals SF formation, indicating the nucleation of a leading 90° partial dislocation having a projected Burgers vector (S to F) of $a/6\langle 112\rangle$. Additionally, the persistence of the SF indicates a lack of trailing 30° partial dislocation formation following nucleation of the leading 90° partial dislocation, thereby preventing dislocation reaction and annihilation of the SF according to Eq. (S3).